Simultaneous determination of continental surface emissivity and temperature from NOAA 10/HIRS observations: Analysis of their seasonal variations

A. Chédin, E. Péquignot, S. Serrar, N. A. Scott

Simultaneous determination of continental surface emissivity and temperature from NOAA 10/HIRS observations: Analysis of their seasonal variations

A. Chédin, E. Péquignot, S. Serrar, and N. A. Scott

Laboratoire de Météorologie Dynamique, Institut Pierre-Simon Laplace, Ecole Polytechnique, Palaiseau, France

Received 9 April 2004; revised 12 July 2004; accepted 9 August 2004; published 19 October 2004.

[1] Continental surface infrared emissivity strongly depends on the wavelength and on the type of the surface. Emissivity values as low as 0.7 may be observed around 8–10 μm or, at shorter wavelengths, around 4 μm, particularly over desert regions. Satellite observations are very sensitive to emissivity variations: At 11 μm an uncertainty as small as 2% may lead to a variation of up to 0.5K in brightness temperature. An accurate and coherent, i.e., simultaneous, determination of surface temperature and emissivity is essential to greatly improve the estimation of the longwave surface energy budget and, consequently, to improve the performance of surface-atmosphere interaction models. On the basis of a space differential approach and a nonlinear regression inference method, 4 years of NOAA 10 observations (July 1987 to June 1991) over northern Africa (5°N–30°N and 20°W–60°E) have been interpreted in terms of surface emissivity at three wavelengths, namely, 11.1 μm, 8.3 μm, and 4 μm, corresponding to atmospheric windows, and surface temperature, actually, "skin" temperature. Emissivity maps at a resolution of $1° \times 1°$ and 1 month reveal strong signatures of sand at 8.3 and 4.0 μm and of carbonates at 11.1 μm. Time series of zonal means may bring into evidence important seasonal variations as, for example, over regions of savannas: from 5% at 11.1 μm (peak to peak) to 15% at 4 μm. They are shown to be in phase with the precipitation and 1 month ahead of the Normalized Difference Vegetation Index time series. The mean uncertainty may be theoretically estimated on the order of less than 2% for the emissivity at 11.1 μm and of 1.6K for the surface temperature. *INDEX TERMS:* 3322 Meteorology and Atmospheric Dynamics: Land/atmosphere interactions; 3337 Meteorology and Atmospheric Dynamics: Numerical modeling and data assimilation; 3360 Meteorology and Atmospheric Dynamics: Remote sensing

Citation: Chédin, A., E. Péquignot, S. Serrar, and N. A. Scott (2004), Simultaneous determination of continental surface emissivity and temperature from NOAA 10/HIRS observations: Analysis of their seasonal variations, *J. Geophys. Res.*, *109*, D20110, doi:10.1029/2004JD004886.

1. Introduction

[2] Because a large part of the surface longwave radiation is directly lost in space within thermal infrared windows, surface as well as top of the atmosphere radiative budgets are significantly influenced by the hemispherical surface emissivity (i.e., integrated over the hemisphere). Hemispherical surface emissivity and longwave upwelling surface radiation are proportional: A 5% error in hemispherical emissivity (from 0.95 to 1.0, for example) approximately corresponds to a 5% error in the integrated longwave upwelling surface radiation (about 15 Wm^{-2}) [*Prabhakara and Dalu*, 1976; *Ogawa et al.*, 2003]. It has also been shown that accounting properly for the channel surface emissivity in the solution of the radiative transfer equation inverse problem substantially improves the retrieved meteorological profiles (temperature, moisture) and cloud characteristics [*Plokhenko and Menzel*, 2000].

[3] In the infrared, sea surface emissivity variations are well known [*Masuda et al.*, 1988] and are within a few percent. Land surface emissivities display much larger variations depending on the soil type and moisture content (and, consequently, on the vegetation), and on the wavelength. Bare soils and desert regions may show emissivity values as low as 0.7 because of the so-called "restrahlen" effect [*Hanel et al.*, 1972] due to strong infrared quartz sand emissivity spectral signatures.

[4] Interpretation of window channel radiances in terms of surface emissivity and temperature is not straightforward because of the strong mixing of their signals in the radiative transfer equation. For that reason, most studies aiming at retrieving one of these variables from satellite observations have used a priori information on the other or have established empirical constraints [*Liang*, 2001]. The method developed here is original in the sense that both variables are determined simultaneously through a nonlinear regres-

0148-0227/04/2004JD004886

sion inference scheme. The method is applied to 4 years of National Oceanic and Atmospheric Administration (NOAA 10) polar satellite observations from July 1987 to June 1991 over northern Africa (5°N–30°N and 20°W–60°E), mostly characterized by desert regions, but also by savanna and tropical forest at the southern edge.

2. Satellite Data

[5] The Television and InfraRed Operational Satellite-Next generation (TIROS-N) Operational Vertical Sounder (TOVS) has been flown aboard the NOAA polar meteorological satellites since 1978 [*Smith et al.*, 1979]. The TOVS consists of three passive vertical sounding instruments: the High-Resolution Infrared Radiation Sounder (HIRS-2), a radiometer with 19 channels in the infrared band and one in the visible band; the Microwave Sounding Unit (MSU), a microwave radiometer with four channels in the vicinity of 55 GHz; and the Stratospheric Sounding Unit (SSU), a pressure-modulated infrared radiometer with three channels near 15 μm. Only HIRS and MSU data are used here. Scan widths are approximately 2200 km wide, providing global coverage every 12 hours. HIRS-2 measures atmospheric and/or surface emission in seven channels located around 15.0 μm, five located around 4.3 μm, one 11.1 μm window channel. Three water vapor sounding channels are located at 8.3 μm, 7.3 μm, and 6.7 μm, the first one, relatively transparent, measuring close to the surface. Ozone and surface emission is measured in one 9.6 μm window channel, surface emission and reflected solar radiation in two window channels at 4.0 μm and 3.7 μm, and reflected solar radiation in one visible channel. The MSU measures atmospheric emission in three 55-GHz O_2 channels and surface and atmospheric emission in one 50 GHz window channel.

[6] Retrieving thermodynamic atmospheric and surface variables, like temperature and water vapor profiles, cloud and surface characteristics, goes through the inversion of the radiative transfer equation. The Improved Initialization Inversion (3I) method [*Chédin et al.*, 1985; *Scott et al.*, 1999] was developed at Laboratoire de Météorologie Dynamique (LMD) for this purpose and applied, within the frame of the NOAA–NASA Pathfinder program, to the reanalysis of more than 13 years of observations of the platforms NOAA 10, NOAA 11, and NOAA 12. The spatial resolution of the 3I retrievals is a compromise between the spatial resolution of the HIRS and MSU sounders. A 3 × 2 (at the edges of an orbit), or 3 × 3, or 3 × 4 (at nadir) array of HIRS spots is grouped together to form a so-called "3I-box" and then collocated with the nearest MSU spot(s). Such boxes represent a surface of nearly 100 × 100 km^2, and 3I retrievals are performed for each array. Important auxiliary information is stored in each box as the land-sea and day-night flags, the surface elevation, the satellite viewing angle, and the clear-cloudy flag for each HIRS spot. Clouds are detected at the HIRS spatial resolution (about 18 km at nadir) by a succession of numerous multispectral threshold tests [*Wahiche et al.*, 1986; *Stubenrauch et al.*, 1996, 1999]. An important part of the cloud detection is the use of simultaneous MSU measurements. Owing to its good spectral sampling (19 infrared channels from 15 μm to 3.7 μm), HIRS is very sensitive to most clouds and, in particular, to cirrus clouds. For example, in the tropics, up to 20% more cirrus are identified by TOVS than by the International Satellite Cloud Climatology Project (ISCCP) [*Stubenrauch et al.*, 1999]. All clear spots (at least 60% clear spots are required within a box to be declared clear) are averaged within each box and surface temperature/emissivity simultaneous retrieval is performed for the resulting averaged brightness temperature values.

Table 1. Sensitivity Statistics on the 872 TIGR Tropical Atmospheres of HIRS Window Channels to Changes in Surface True Emissivity for a Variation $\Delta\varepsilon = -0.05$[a]

Channel	Wavelength, μm	Mean, K	Standard Deviation, K
8	11.1	−1.30	0.71
10	8.3	−0.64	0.30
18	4.0	−1.05	0.09

[a]Sensitivity temperatures are given in kelvins. TIGR is Thermodynamic Initial Guess Retrieval.

[7] Table 1 lists the mean sensitivities of the three main HIRS window channels measuring at 11.1 μm (channel 8), 8.3 μm (channel 10), and 4.0 μm (channel 18) to surface emissivity variation (numbers computed from the Automatized Atmospheric Absorption Atlas (4A) model in its latest version [*Scott and Chédin*, 1981] (see also http://ara.lmd.polytechnique.fr) with up to date spectroscopy, using a set of representative tropical atmospheric situations [*Garand et al.*, 2001]). All three channels show an important sensitivity to emissivity, channel 8 being the most sensitive and channel 10 the least.

[8] HIRS window channels are well adapted to observing prevalent surface minerals. The most intense spectral feature of silicates occurs between 8 and 10 μm and is due to fundamental asymmetric O-Si-O stretching vibrations. Weaker bands in quartz spectra between 12 and 15 μm have been attributed to symmetric O-Si-O stretching vibrations [*Farmer*, 1974]. An additional weak band is seen between 3 and 5 μm which may be used for the spectral identification of fine particulate minerals and rocks, where it is quite prominent [*Salisbury et al.*, 1987]. Because the major component of sand is silicate, HIRS channels 10 and 18, centered at 8.3 and 4.0 μm, respectively, are therefore sensitive to sandy soils. However, the intensity of silicate vibration band is lower at 4 μm than at 8.3 μm, and the influence of water and OH vibration features occurring between 2 and 7 μm [*Salisbury et al.*, 1991] both contribute to the lower sensitivity of HIRS channel 18 to sandy soils. The strongest bands of carbonates are due primarily to fundamental internal molecular vibration bands of the CO_3 ion [*Farmer*, 1974]. Carbonates typically display a strong band near 7 μm because of asymmetric C-O stretching vibrations and weaker bands near 11.4 and 14.3 μm because of bending modes which can be seen in the spectrum of calcite and dolomite, the major components of carbonate soils. The HIRS channel 8 is therefore sensitive to such soils. These spectral signatures, from the Advanced Spaceborne Thermal Emission and Reflection Radiometer (ASTER) spectral library (available at http://speclib.jpl.nasa.gov), are shown on Figure 1. From the same reference, laboratory measurements over a large variety of soils show emissivity values ranging from 1.0 to 0.9 for channel 8, and from 1.0 to 0.7 for channels 10 and 18.

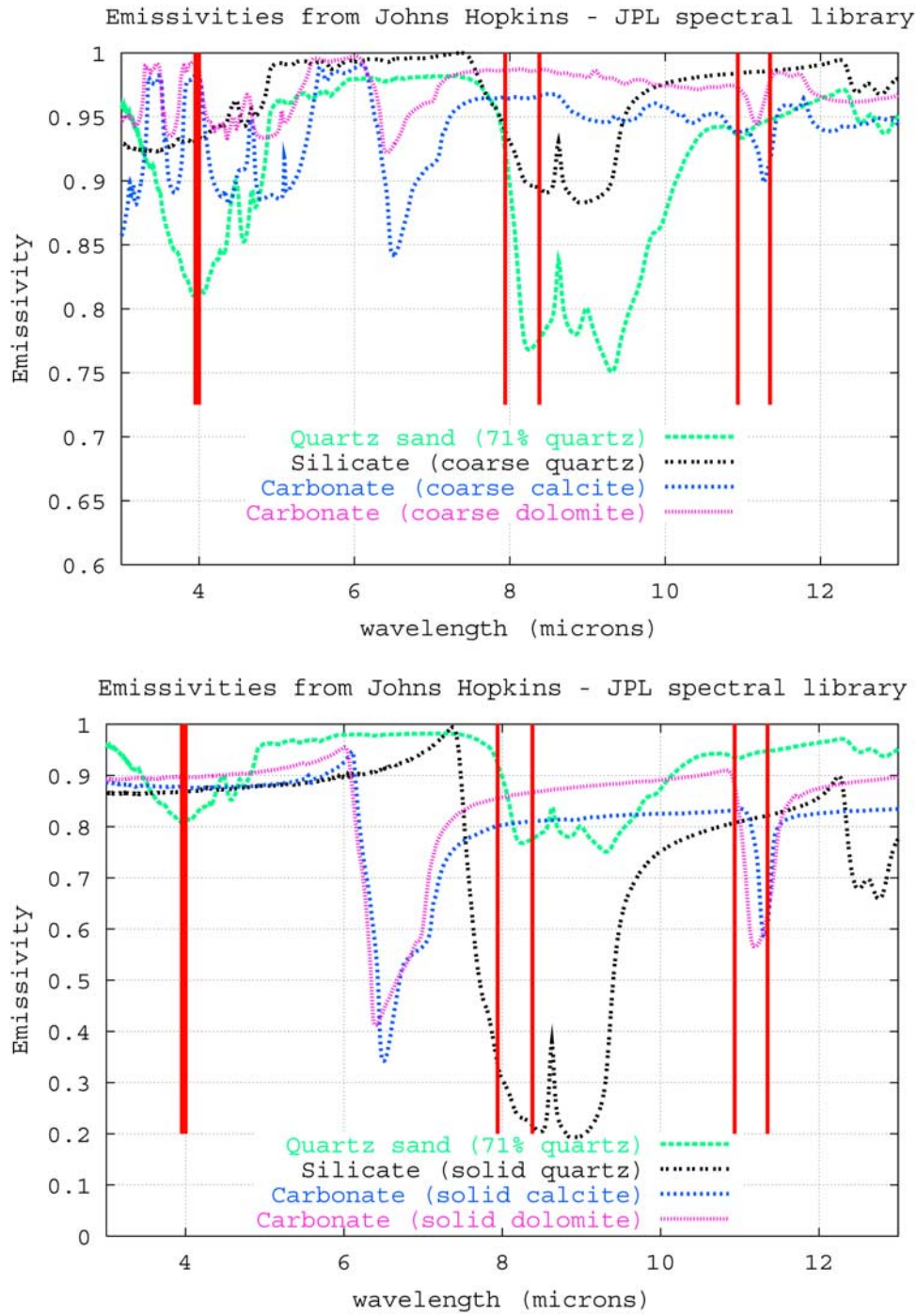

Figure 1. Emissivity of different mineral samples as a function of wavelength. Samples referred to as coarse have a typical particle size between 50 and 250 μm. Vertical red lines delimit the spectral bands of HIRS channels 8, 10, and 18, centered at 11.1 μm, 8.3 μm, and 4.0 μm, respectively. Reproduced from the ASTER Spectral Library through the courtesy of the Jet Propulsion Laboratory, California Institute of Technology, Pasadena, California. Copyright © 1999, California Institute of Technology. All rights reserved.

[9] Other HIRS longwave surface sensitive channels (channels 6 at 13.7 μm and 7 at 13.4 μm), also sensitive to the lower troposphere temperature, correspond to an almost constant emissivity value of 0.98 whatever the soil type is (ASTER spectral library, available at http://speclib.jpl.nasa.gov). For that reason, they are used here to constrain the surface emissivity/temperature inference scheme.

[10] The main difficulty raised by the simultaneous retrieval of surface emissivity and temperature lies in the fact that the number of unknowns to be retrieved, the predictands, is larger than the number of knowns (the

predictors). Observing a given $1° \times 1°$ area (a 3I box) at N wavelengths provides N knowns (the N channel brightness temperatures) with $N + 1$ unknowns: the N channel emissivities and the surface temperature. If we now consider two consecutive boxes and make the assumption that these two boxes have the same surface emissivity and distinct surface temperatures, the number of knowns come to $2N$, when the number of unknowns is $N + 2$: the N channel emissivities, common to the two boxes, and the two surface temperatures. If $N = 2$, the system becomes exactly determined. For three consecutive boxes, it is easy to see that there are $3N$ knowns and $N + 3$ unknowns, that is to say 9 knowns and 6 unknowns if we consider three wavelengths. The system becomes overdetermined. This is what has been done here. We could have made the assumption that the three boxes have the same surface temperature and distinct emissivities. Our choice was dictated by the greater sensitivity of the channel radiances to the surface temperature than to the emissivity. It is worth pointing out that the three consecutive boxes selected are viewed under the same satellite viewing angle.

3. Inference Method

[11] Under clear-sky conditions (i.e., no clouds, no aerosols) and under the assumption of local thermodynamic equilibrium, the calculation of the monochromatic radiance $I(\nu, \theta)$ emitted by the atmosphere at the spectral frequency ν in the direction θ leads to the radiative transfer equation which may be written in the following way:

$$I(\nu,\theta) = \varepsilon_s(\nu,\theta)\tau_s(\nu,\theta)B(T_s,\nu) + \int_{\tau_s(\nu,\theta)}^{1} B(T(\tau),\nu)d\tau + \rho(\nu,\theta)\tau_s(\nu,\theta) \cdot \int_{\tau_s(\nu,\theta)}^{1} B(T(\tau'),\nu)d\tau' \quad (1)$$

In equation (1), $\tau(\nu, \theta)$ stands for the (monochromatic) transmission function between the satellite and the current level, $\tau'(\nu, \theta)$ stands for the transmission between the surface and the current level, and $\tau_s(\nu, \theta)$ stands for the transmission between the satellite and the surface. Here $\varepsilon_s(\nu, \theta)$ represents the directional emissivity of the surface and $\rho(\nu, \theta)$ the directional reflectance of the surface, assumed to be Lambertian. T_s is the skin surface temperature and $B(T, \nu)$ is the usual Planck function. The first and the second terms of equation (1) describe the upwelling radiance emitted by the surface of the Earth and its atmosphere through the atmosphere. The third term corresponds to the downwelling radiance emitted by the atmosphere and reflected by the surface back to the satellite. Use is made here of the directional reflectance of the surface instead of the bidirectional one because account has to be taken of the radiance downwelling from the atmosphere from all directions and reflected at the satellite viewing angle θ [*Nicodemus*, 1965]. The equilibrium maintenance with conservation of energy (Kirchhoff's law) leads to $\rho(\nu, \theta) = 1 - \varepsilon_s(\nu, \theta)$. Under the Lambertian assumption, the directional emissivity is independent of the viewing angle, i.e., $\varepsilon_s(\nu, \theta) = \varepsilon_s(\nu)$. Therefore the radiative transfer may be written as

$$I(\nu,\theta) = \varepsilon_s(\nu)\tau_s(\nu,\theta)B(T_s,\nu) + \int_{\tau_s(\nu,\theta)}^{1} B(T(\tau),\nu)d\tau + (1-\varepsilon_s(\nu))\tau_s(\nu,\theta) \cdot \int_{\tau_s(\nu,\theta)}^{1} B(T(\tau'),\nu)d\tau' \quad (2)$$

Equation (2) may be simplified by replacing the true emissivity $\varepsilon_s(\nu)$ by an "effective" emissivity $\varepsilon_s^{\text{eff}}(\nu)$, and can then be rewritten as

$$I(\nu) = \varepsilon_s^{\text{eff}}(\nu)\tau_s(\nu)B(T_s,\nu) + \int_{\tau_s(\nu,\theta)}^{1} B(T(\tau),\nu)d\tau \quad (3)$$

From the comparison of equations (2) and (3), it follows that

$$\varepsilon_s^{\text{eff}}(\nu) = \varepsilon_s(\nu) + \frac{(1-\varepsilon_s(\nu))}{B(T_s,\nu)} \int_{\tau_s(\nu,\theta)}^{1} B(T(\tau'),\nu)d\tau' \quad (4)$$

The true emissivity, $\varepsilon_s(\nu)$ may be simply deduced from the effective emissivity as shown by *Heilliette et al.* [2003]. Results given in the following are in terms of effective emissivity, hereafter referred to as "emissivity." It is worth pointing out that ε^{eff} is larger than ε and that the difference between ε^{eff} decreases when ε (or ε^{eff}) tends toward 1, as shown in Table 2. Here we consider effective emissivity because it drastically reduces the time for numerical calculations. Note that quantitative results could be corrected with respect to the difference between effective and true emissivity. Nevertheless, the main patterns and contrasts shown in effective emissivity maps and their seasonal variations will be preserved and slightly amplified.

[12] The difficulty of the interpretation of window channel radiances in terms of surface emissivity and temperature has been accounted for by choosing, instead of simple linear regressions, the more complex way offered by neural network techniques. In particular, such inference techniques allow eventual nonlinearities to be properly taken into account and do not necessitate to explicitly formulate the functional linking the knowns and the unknowns. Here use is made of the Multi-Layer Perceptron (MLP) [*Rumelhart et al.*, 1986]. The MLP network is a nonlinear mapping model composed of parallel processors called "neurons." These processors are organized in distinct layers. The first layer represents the input of the mapping. The intermediate layers are called the "hidden layers." These layers are connected via neural links: two neurons i and j between two consecutive layers have synaptic connections associated with a synaptic weight w_{ij}. Each neuron i executes two simple operations. First, it makes a weighted sum of its inputs z_i; this signal is called the activity of the neuron:

$$a_i = \sum_{i \in \text{Inputs}(j)} w_{ij} z_i \quad (5)$$

Table 2. Mean Calculated Effective Emissivity (ε_{eff}) on the 872 TIGR Tropical Atmospheres of HIRS Window Channels 8, 10, and 18 for a Given True Emissivity (ε)

HIRS Channel 8 at 11.1 μm			HIRS Channel 10 at 8.3 μm			HIRS Channel 18 at 4.0 μm		
ε	ε_{eff}	$\varepsilon_{eff} - \varepsilon$	ε	ε_{eff}	$\varepsilon_{eff} - \varepsilon$	ε	ε_{eff}	$\varepsilon_{eff} - \varepsilon$
0.900	0.917	0.017	0.700	0.773	0.073	0.700	0.719	0.019
0.950	0.958	0.008	0.850	0.886	0.036	0.850	0.860	0.010
1.000	1.000	0.000	1.000	1.000	0.000	1.000	1.000	0.000

Then, it transfers this signal to its output through a so called "transfer function," often a sigmoidal function such as $\sigma(a) = \tanh(a)$. The output z_j of neuron j in the hidden layer is then given by

$$z_j = \sigma(a_j) = \sigma\left(\sum_{i \in \text{Inputs}(j)} w_{ij} z_i\right) \quad (6)$$

Given a neural architecture (with specified number of layers, neurons and connections), all the information of the network is contained in the set of synaptic weights $W = \{w_{ij}\}$. The learning algorithm is the optimization technique that estimates the optimal network parameters W by minimizing a positive-definite cost function which measures, for a set of representative patterns for which inputs and outputs are known (the learning set), the mismatch between the neural net outputs and the desired outputs. This enables one to approximate the desired function as closely as necessary by the neural mapping. Here the Error Back-Propagation algorithm [*Rumelhart et al.*, 1986] is used to minimize the cost function. It is a gradient descent algorithm well adapted to the MLP hierarchical architecture because the computational cost is linearly related to the number of parameters. To avoid being trapped in local minima during the minimization of the cost function, stochastic steepest descent is used. The learning step is made sample by sample chosen iteratively and stochastically in the learning data set.

[13] Training of the MLPs is performed using the Thermodynamic Initial Guess Retrieval (TIGR) climatological library of about 2300 representative atmospheric situations selected by statistical methods from 80,000 radiosonde reports [*Chédin et al.*, 1985; *Chevallier et al.*, 1998]. Each situation is described by its temperature, water vapor and ozone profiles (40 levels from 1013 hPa to 0.05 hPa). The ozone profile is specified from the UGAMP ozone climatology [*Li and Shine*, 1995], taking into account the latitude, longitude and time of each situation archived in TIGR. For each atmospheric situation, a surface temperature is generated as the sum of the temperature of the atmosphere at the lowest level and a random number with zero mean and a standard deviation of 4K. This insures that 99% of the skin temperatures chosen are between $T_{\text{air-ground}} - 12\text{K}$ and $T_{\text{air-ground}} + 12\text{K}$. We have considered that this variability of skin temperature with respect to air temperature at the ground was sufficiently representative. Finally, the situations in TIGR are stratified by a hierarchical ascending classification into five air mass types (tropical, temperate –midlat1–, cold temperate and summer polar –midlat2–, northern hemisphere very cold polar –polar1–, winter polar –polar2–), depending of their virtual temperature profiles [*Achard*, 1991; *Chédin et al.*, 1994].

Table 3. Statistics for the 42 Networks at the End of the Learning Process[a]

	T_{s1} (K)	T_{s2} (K)	T_{s3} (K)	$\varepsilon(8)$	$\varepsilon(10)$	$\varepsilon(18)$
Standard deviation (mean)	0.88	0.88	0.89	0.014	0.021	0.036
Bias (maximum)	0.018	0.020	0.020	0.0006	0.0007	0.0005

[a] T_{s1}, T_{s2}, and T_{s3} stand for the surface temperature of the three boxes, and $\varepsilon(8)$, $\varepsilon(10)$, $\varepsilon(18)$ stand for the effective emissivity of HIRS channels 8, 10, and 18.

[14] Clear sky transmittances, brightness temperatures and Jacobians (partial derivatives of the brightness temperature with respect to temperature, gas concentration, surface temperature and emissivity, etc.) for all TOVS sounding channels are then computed for each situation archived using the fast line-by-line 4A model. Calculations are performed for 10 viewing angles, between 0° (nadir) and 60° (the maximum value for angular scanning; the present study has been limited to 40°), for 19 values of surface pressure (up to about 500 hPa) for elevated terrains, and for two surface types: sea (not used here) and land [*Chédin et al.*, 1985]. A fixed emissivity of 0.98 is specified for all channels over land, except for the channels at 4.3 μm, for which the emissivity is 0.97. These results are also stored within the TIGR data set. It is worth pointing out that TIGR is not primarily sensitive to the relative quality of the radiosoundings sampled in it but only to their representativeness and plausibility. In fact, it is sensitive to the quality of the relationship between thermodynamic quantities and radiative quantities.

4. Training Phase and Validation

[15] In consideration of the geographical area selected (5°N–30°N and 20°W–60°E), only the 872 tropical situations of TIGR have been retained. For each such situation (randomly drawn at each iteration of the network convergence process), the key predictors are the brightness temperatures of the HIRS window channels 8 (11.1 μm), 10 (8.3 μm), and 18 (4.0 μm). The solution is constrained by adding the brightness temperatures of channels 6 (13.7 μm) and 7 (13.4 μm), sounding the temperature of the lowest atmospheric layers, as well as their differences with each key channel (8, 10, 18), giving 11 entries for each TIGR situation selected. These differences have been shown to greatly help deconvolve emissivity and temperature and to speed up the convergence process. Then, because TIGR brightness temperatures correspond to fixed values of the

Table 4. Statistics for the 100 Situations Selected From ECMWF-ERA40 Multiplied by 100 Combinations of Emissivities Validation[a]

	T_{s1}, K	T_{s2}, K	T_{s3}, K	$\varepsilon(8)$	$\varepsilon(10)$	$\varepsilon(18)$
Standard deviation	1.58	1.57	1.57	0.018	0.028	0.059
Bias	0.029	0.044	0.082	−0.0006	−0.0043	−0.0050

[a] T_{s1}, T_{s2}, and T_{s3} stand for the surface temperature of the three boxes, and $\varepsilon(8)$, $\varepsilon(10)$, and $\varepsilon(18)$ stand for the effective emissivity of HIRS channels 8, 10, and 18, respectively.

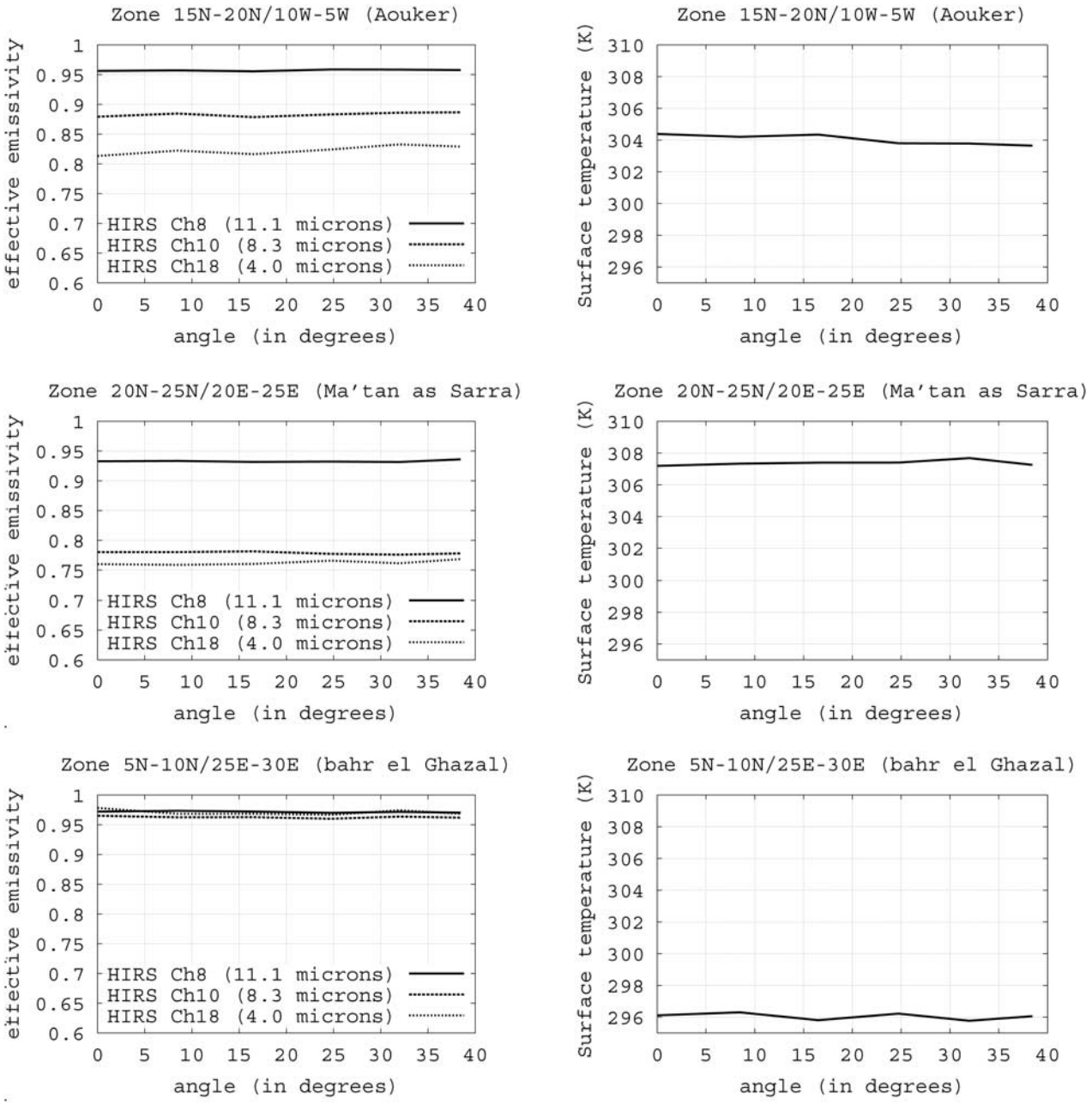

Figure 2. HIRS channels 8, 10, and 18 retrieved surface (left) emissivity and (right) temperature as a function of the viewing angle. Plotted values result from the averaging of all individual retrievals (one item), viewing angle by viewing angle, over the 2 months of July and August (from 1987 to 1991): (top) 15°N–20°N/10°W–5°W (Aouker, zone 1, 800 items); (middle) 20°N–25°N/20°E–25°E (Ma'tan as Sarra, zone 2, 1300 items); and (bottom) 5°N–10°N/25°E–30°E (bahr el Ghazal, zone 3, 300 items).

emissivity, each entry is adapted to randomly drawn values of each channel emissivity, within the ranges indicated above, using the emissivity Jacobians. To over determine the system (see section 2), each situation selected is associated with two other situations simulating the set of the three closest in space situations. They are selected through a pattern recognition approach within TIGR using a simple Euclidian distance in brightness temperature [*Chédin et al.*, 1985]. Consequently, the total number of entries (input layer) comes to 33 (3 channels times the 11 above entries). Finally, noise equivalent temperature (NEΔT) is added to the input brightness temperatures in order to account for the instrument and model noises. The output layer (the predictands) is made of the three emissivities (one for each key channel) and the three surface temperatures (one for each of the set of three).

[16] A total of 42 MLPs have been trained, one for each viewing angle (here, 7, up to about 40° to avoid orbit edges) and for each surface elevation (6, up to about 875 hPa, the value to which the present study has been limited). After several tests, each MLP has been given two hidden layers, 66 neurons for the first one and 24 for the second. Statistics

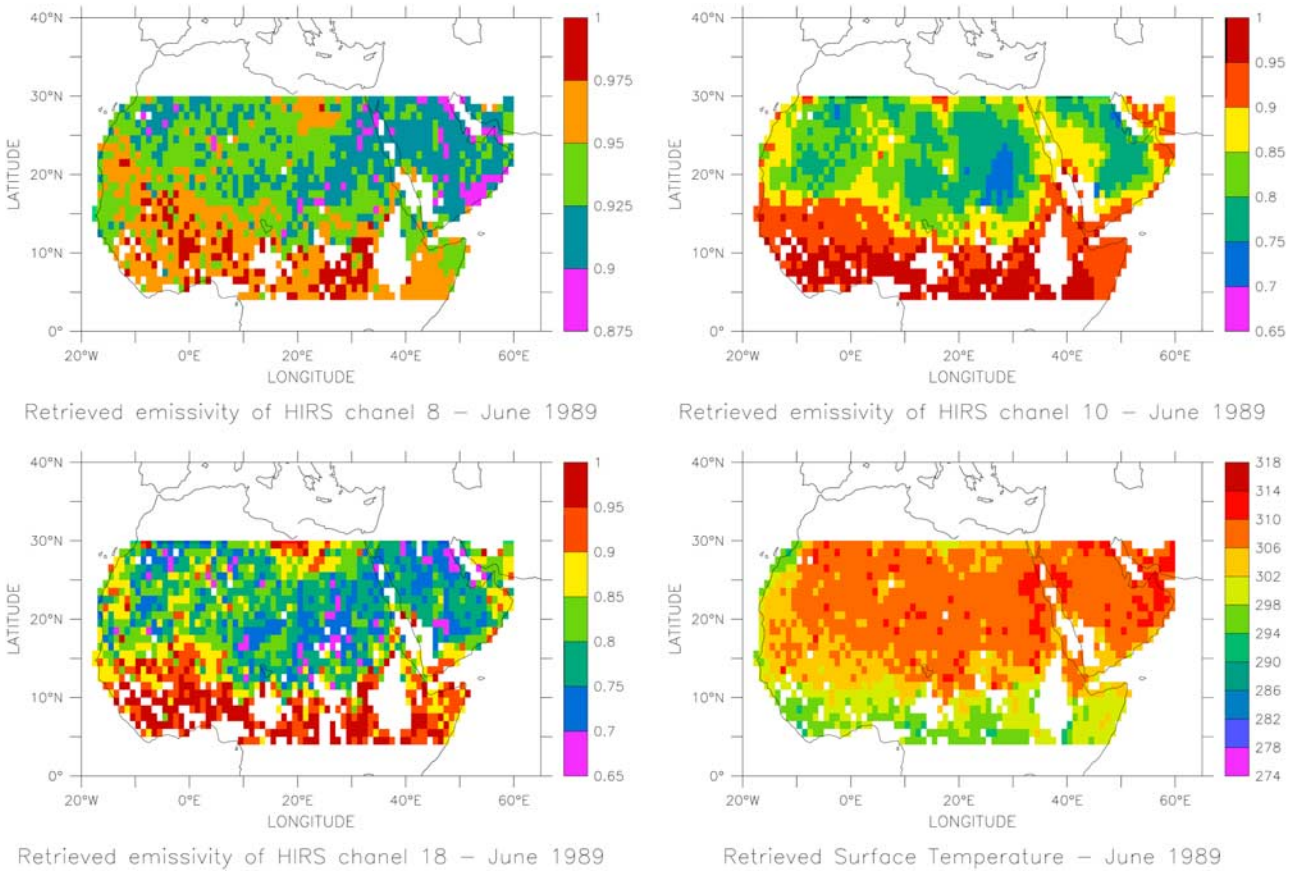

Figure 3. Results for the month of June 1989: (top left) emissivity of channel 8 (11.1 μm), with range [0.875, 1]; (top right) emissivity of channel 10 (8.3 μm), with range [0.65, 1]; (bottom left) emissivity of channel 18 (4.0 μm), with range [0.65, 1]; and (bottom right) surface temperature (K), with range [274, 318].

for the surface emissivities and temperatures obtained at the end of the learning process (mean over the 42 networks) are given in Table 3.

[17] In order to evaluate the accuracy of the neuronal inversion model and to test the ability to generalize of the MLPs, we have selected, from the European Centre for Medium-Range Weather Forecasts reanalysis (ECMWF-ERA40) radiosonde archive, a set of 100 radiosoundings describing atmospheric situations completely independent from the training data set. The radiosoundings have been chosen under clear-sky nighttime conditions within the region considered and the time period from July 1987 to June 1991. As for the training data set, each situation selected was associated with two other situations from the same archive, simulating the set of the three closest situations in space. Corresponding HIRS channel brightness temperatures were then calculated using the 4A line-by-line model for each of the 300 (3 × 100) atmospheric situations. Then, a set of 100 combinations of randomly chosen HIRS channel 8, 10 and 18 emissivities (within the ranges indicated in section 2) was created. By using the same method as for constituting the training database, the brightness temperatures calculated by 4A for the 300 ERA40 atmospheric situations were scaled to each emissivity combination to take into account the emissivity variability. Results for the 100 selected situations × 100 combinations of emissivities cases processed are given in Table 4 using the neural network educated for nadir viewing conditions and for a surface pressure equal to 1013 hPa. They are representative of the accuracy which may be expected from the method. From Table 4 one can see that biases are quite law. Standard deviations are equal for the three output surface temperatures of the value of 1.6K. They differ for the surface emissivities, best results (less than 0.02) being obtained for channel 8, then 10 (of the order of 0.03) and 18 (of the order of 0.06).

5. Application to NOAA 10 Observations

[18] Four years of NOAA 10 observations (from July 1987 to June 1991) have been processed and interpreted in terms of monthly mean surface emissivity and temperature, for the region 5°N–30°N and 20°W–60°E.

5.1. Radiation Model Bias Removal

[19] Because the MLPs are trained with simulated data, their application to real data implies that possible brightness temperature systematic biases between simulations and observations have been eliminated. This may be done by comparing simulations and observations for a set of collocated satellite and radiosonde data. Collocations are from the so-called "DSD5" NOAA/National Environmental Sat-

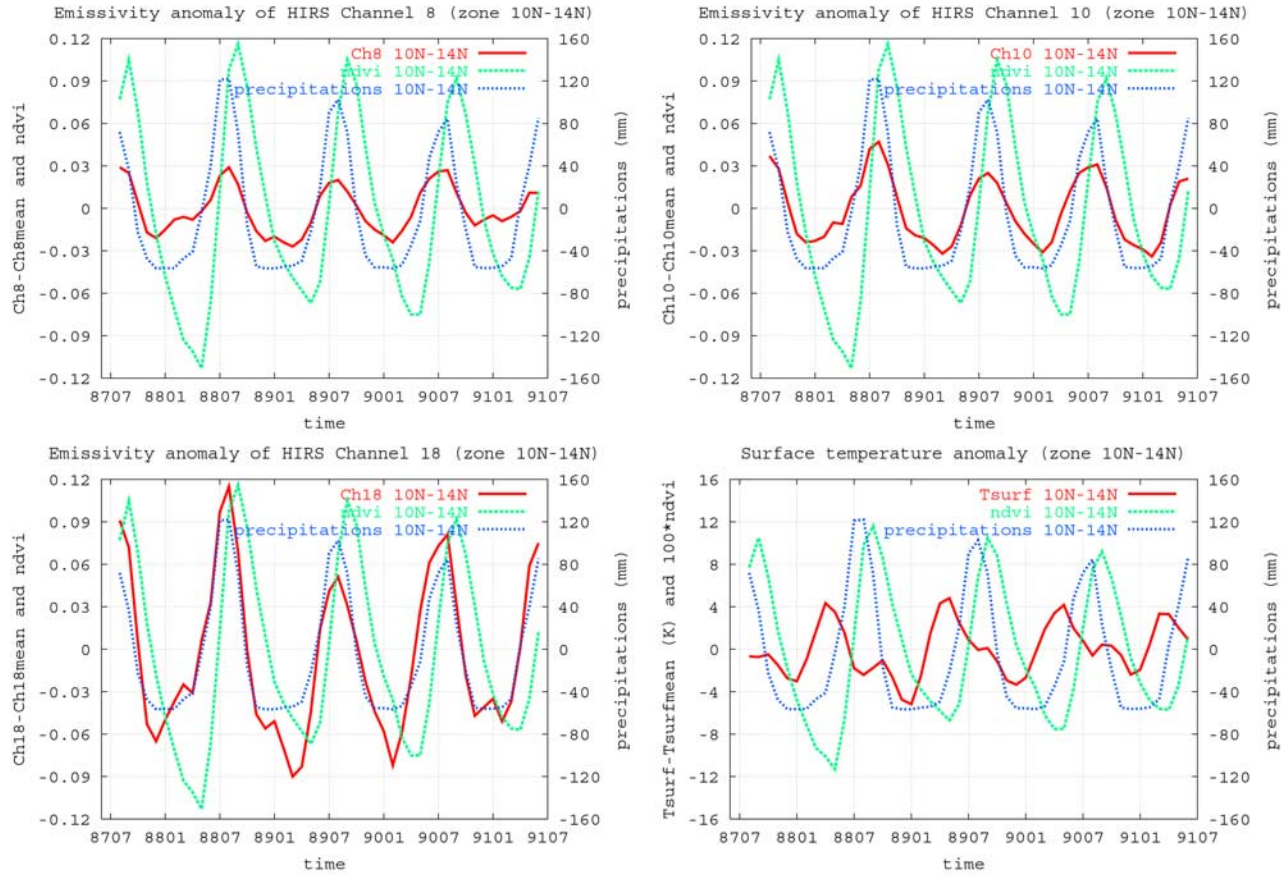

Figure 4. Seasonal variations with respect to the mean (anomaly) of the retrieved variables (in red): (top left) channel 8 emissivity, (top right) channel 10 emissivity, (bottom left) channel 18 emissivity, and (bottom right) surface temperature. Green indicates NDVI anomaly (multiplied by 100 for surface temperature plot); blue indicates precipitation anomaly. Region shown is 10°N–14°N, 10°W–30°E.

ellite Data and Information Service (NESDIS) collocation archive [*Uddstrom and McMillin*, 1994]. For each channel, the systematic bias is obtained by averaging the difference between simulations and observations over the whole time period considered. Brightness temperature systematic biases are computed separately over sea and over land. Daytime observations are not considered because of possible contamination by solar radiation of the short-wavelength channels. As a consequence, with NOAA 10, observations are at around 7:30 P.M. local time.

5.2. Results

[20] Given an observation, i.e., a "3I box" of 1° × 1° (the "reference box") with latitude (Lat) and longitude (Lon), two spatially close clear situations are searched within an area defined by Lat ± 2° and Lon. Among all possible boxes, the two selected ones (1) are the closest, (2) correspond to the same viewing angle as that of the original box, and (3) have a surface pressure (terrain elevation) not differing by more than 28 hPa from that of the original box. All three boxes (the reference box and its two associated ones) must have a surface pressure not smaller than 875 hPa. Surface temperature and emissivities for each channel are then retrieved for each such set of three boxes: Results kept are those of the "reference box." Monthly means are then computed at the 1° × 1° grid.

[21] Such monthly means aggregate retrievals coming from observations made at different viewing angles, implying that the dependence of the emissivity on the viewing angle is negligible. Moreover, at our spatial resolution, the mean surface observed may reasonably be expected to be Lambertian. To verify this assertion, we first selected several areas on the basis of their surface homogeneity, six mostly over desert, and one over a region of savannas and tropical grassland. Then, for each of these areas, we collected all the individual retrievals (or items) obtained for the whole time period of 4 years, separately for each month for the sake of homogeneity with respect to potential seasonal variations, and produced statistics for the channel emissivities and for the temperature (mean and standard deviation), viewing angle by viewing angle. Results for the two months of July and August (to increase the number of items), and for the three areas (over the seven studied): 15°N–20°N/10°W–5°W (Aouker, zone1, 800 items), 20°N–25°N/20°E–25°E (Ma'tan as Sarra, zone 2, 1300 items), 5°N–10°N/25°E–30°E (bahr el Ghazal, zone 3, 300 items) are shown on Figure 2. It clearly confirms, for the three channels, the absence of dependence of the emissivity on the viewing angle. Zone 1, with some savannas southward, shows larger emissivities than zone 2, purely desert, when zone 3, with more vegetation, shows almost unit emissivity for the three

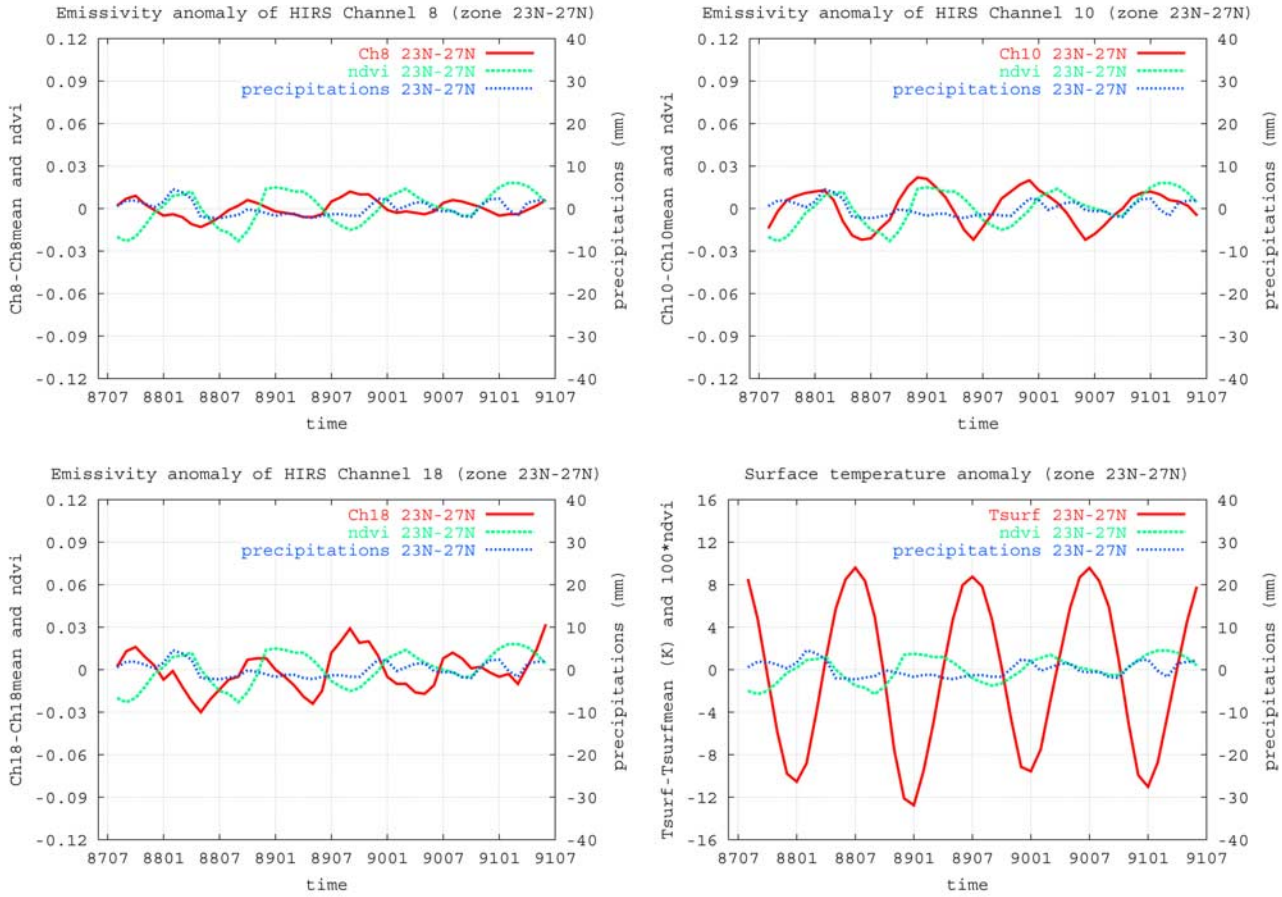

Figure 5. Same as Figure 4 for the region 23°N–27°N, 10°W–30°E.

channels. These results are representative of the other areas and other months studied.

[22] Figure 3 displays the results obtained for the emissivity of the three window channels and for the surface temperature for the month of June 1989. On these maps, blank areas correspond to either rejections due to too small a number of retrievals obtained for the grid point considered (due, for example, to persistent clouds or aerosols), or to a mean surface pressure smaller than 875 hPa as, for example, for the range of Ethiopian mountains around 10°N–38°E. As expected from the smaller sensitivity of channel 18 at 4 μm to emissivity variations, the corresponding map displays a larger noise. Whatever the frequency is, Figure 3 shows higher emissivities and lower surface temperatures at latitudes south of 15°N than at latitudes north of 15°N, which is in agreement with the nature of the terrain: mostly desert north of about 15°N and more and more vegetated south of 15°N. Nighttime observations from NOAA 10 made at 7:30 P.M. after a long insolation time period explain the high surface temperatures retrieved over the desert. Desert areas are characterized by low emissivity values for both channels 10 and 18, located on two sand emissivity spectral signatures (ASTER spectral library available at http://speclib.jpl.nasa.gov). Lowest values, of the order of 0.7, are observed for the Sudan desert (17°N to 23°N and around 25°E to 30°E). By considering the relationship between true and effective emissivity, an effective emissivity of 0.7 at 8.3 μm should correspond to a true emissivity of about 0.6–0.65. These values observed at 8.3 μm overt desert regions are in agreement with values observed at 9.1 μm [*Ogawa et al.*, 2003] considering the fact that spectral emissivity signature of quartz sand soils at 8.3 μm and 9.1 μm are equivalent, as shown on Figure 2. Other features are identified, as, for example, the Tibesti (21°N–17°E), Hoggar (23°N–6°E), or Darfour (14°N–24°E) mountains associated with emissivities of the order of 0.85 to 0.90, larger than those of pure sand areas. East of Oman and South of Yemen, emissivity values between 0.90 and 0.95 well correspond to mountainous vegetation identified on current vegetation maps. At 11.1 μm, as expected, the emissivity map displays smaller but almost equally significant variability with, in particular, a few areas where values less than 0.9 are observed, for example, south of Yemen and Oman. From the ASTER spectral library (see above), such signatures may be attributed to carbonates (C. Prigent, personal communication, 2004).

[23] Seasonal variations with respect to the mean over the 4 year period (or anomalies) of the retrieved surface emissivity and temperature are shown on Figures 4 and 5 for two very contrasted areas, the first one, 10°N–14°N, 10°W–30°E, with vegetation sensitive to the precipitation seasonal cycle (Figure 4), and the second one, (23°N–27°N, 10°W–30°E), mostly desert, with very low precipitations (Figure 5). The seasonal variations (anomaly) of the normalized difference vegetation index (NDVI) and of the precipitations are also plotted on Figures 4 and 5.

[24] NDVI is derived from broadband red and near-infrared reflectance measurements made by the advanced very high resolution radiometer (AVHRR) aboard the NOAA polar-orbiting platforms. It is computed as

$$\mathrm{NDVI} = (\mathrm{ch2} - \mathrm{ch1})/(\mathrm{ch2} + \mathrm{ch1}) \quad (7)$$

where ch2 and ch1 are the radiances in the near-infrared and red portions of the spectrum, respectively. NDVI and precipitation anomalies are from ftp://daac.gsfc.nasa.gov/data/inter_disc/biosphere/avhrr_ndvi/ and http://daac.gsfc.nasa.gov, respectively. Figure 4, for the region (10°N–14°N, 10°W–30°E), shows large seasonal variations of the emissivities, of the precipitation, and of the NDVI. The former two are exactly in phase, when the latter is delayed by 1 month. This is due to the sensitivity of the surface emissivity to the soil moisture and to the fact that the NDVI essentially responds to chlorophyll of the vegetation leaves, appearing after the occurrence of the precipitation. As expected for a region close to the equator, surface temperature displays relatively modest variations (±4K). The situation is reversed for the desert region (23°N–27°N, 10°W–30°E) showing small seasonal variations of the emissivities and, as expected for a region more distant from the equator, much larger surface temperature variations (±10 K) (Figure 5). Precipitation and NDVI anomalies are too small to be significant.

6. Conclusions

[25] Because of the high sensitivity of longwave outgoing radiances in window channels to surface emissivity, its accurate knowledge is required for numerous studies as the determination of the longwave radiative budget, or the retrieval of meteorological profiles and cloud characteristics from infrared vertical sounders. The situation is most critical over land where the emissivity variability is large and where values as low as 0.7 may be observed. This was confirmed by the present study of surface emissivity at three window frequencies: 11.1, 8.3, and 4.0 μm corresponding to the HIRS channels 8, 10, and 18, respectively. Surface temperature was simultaneously determined using a spatial differential nonlinear inference scheme, ensuring a good decorrelation of the two variables. Four years of NOAA 10 observations over northern Africa were analyzed, covering the period July 1987 to June 1991. Key results are the following.

[26] 1. The importance of the variability of surface emissivity over deserts (here the Sahara), not only at 8.3 μm and 4.0 μm, corresponding to two sand spectral signatures (values ranging from 0.7 to 0.9, a 4K variation, translated into brightness temperature), but also at 11.1 μm (values from slightly less than 0.90 to 0.975, a more than 3K brightness temperature variation), in part due to carbonate signature, is shown.

[27] 2. The dramatic seasonal variations experienced by emissivity for all three frequencies, in particular over vegetated regions corresponding to steppes and savannas, is shown. Ranges of variation are of the order of ±0.03 at 11.1 and 8.3 μm and ±0.09 at 4.0 μm. They correspond to even larger variations of the true surface emissivity (see comment after equation (4)). These seasonal variations are in phase with the precipitations and ahead of the NDVI index by 1 month.

[28] Such results should help improving models of the Earth surface-atmosphere interaction. Work will continue with the 25 year archive of HIRS data and with the new high spectral resolution vertical sounder Atmospheric Infrared Sounder (AIRS) now flying aboard the NASA/AQUA platform.

[29] **Acknowledgments.** We are happy to thank R. Armante, S. Heilliette, and C. Prigent for their help and fruitful discussions. This work has benefited from the large computing facilities of IDRIS, the computing center of CNRS. Warm thanks are also due to the three anonymous referees for their particularly constructive and helpful comments and criticism.

References

Achard, V. (1991), Trois problèmes clés de l'analyse 3D de la structure thermodynamique de l'atmosphère par satellite. Thèse de doctorat, 168 pp., Univ. Paris 7, Paris.

Chédin, A., N. A. Scott, C. Wahiche, and P. Moulinier (1985), The improved initialization inversion method: A high resolution physical method for temperature retrievals from satellites of the TIROS-N series, *J. Clim. Appl. Meteorol.*, *24*, 128–143.

Chédin, A., N. A. Scott, C. Claud, B. Bonnet, J. Escobar, S. Dardaillon, F. Cheruy, and N. Husson (1994), Global scale observation of the Earth for climate studies, *Adv. Space Res.*, *14*(1), 155–159.

Chevallier, F., F. Cheruy, N. A. Scott, and A. Chédin (1998), A neural network approach for a fast and accurate computation of a long wave radiative budget, *J. Appl. Meteorol.*, *37*, 1385–1397.

Farmer, V. C. (Ed.) (1974), The Infrared Spectra of Minerals, *Mineral. Soc. Monogr.*, *4*, 539 pp.

Garand, L., et al. (2001), Radiance and Jacobian intercomparison of radiative transfer models applied to HIRS and AMSU channels, *J. Geophys. Res.*, *106*, 24,017–24,031.

Hanel, R. A., B. J. Conrath, V. G. Kunde, C. Prabhakara, I. Revah, V. V. Salomonson, and G. Wolford (1972), The Nimbus 4 Infrared Spectroscopy Experiment, *J. Geophys. Res.*, *77*, 2629–2641.

Heilliette, S., A. Chédin, N. A. Scott, and R. Armante (2003), Parameterization of the effect of surface reflection on spectral infrared radiance measurements: Application to IASI, *J. Quant. Spectrosc. Radiat. Transfer*, *86*, 201–214.

Li, D., and K. P. Shine (1995), A 4-dimensional ozone climatology for UGAMP models, *Internal Rep. 35*, UK Univ. Global Atmos. Model. Programme, Natl. Environ. Res. Counc., Swindon, UK.

Liang, S. (2001), An optimization algorithm for separating land surface temperature and emissivity from multispectral thermal infrared imagery, *IEEE Trans. Geosci. Remote Sens.*, *39*, 264–274.

Masuda, K., T. Takashima, and Y. Takayama (1988), Emissivity of pure and sea waters for the model of sea surface in the infrared window region, *Remote Sens. Environ.*, *24*, 313–329.

Nicodemus, F. E. (1965), Directional reflectance and emissivity of an opaque surface, *Appl. Opt.*, *4*, 767–773.

Ogawa, K., T. Schmugge, F. Jacob, and A. French (2003), Estimation of land surface window (8–12 μm) emissivity from multi-spectral thermal infrared remote sensing—A case study in a part of Sahara Desert, *Geophys. Res. Lett.*, *30*(2), 1067, doi:10.1029/2002GL016354.

Plokhenko, Y., and W. P. Menzel (2000), The effects of surface reflection on estimating the vertical temperature-humidity distribution from spectral infrared measurements, *J. Appl. Meteorol.*, *39*, 3–14.

Prabhakara, C., and G. Dalu (1976), Remote sensing of surface emissivity at 9 μm over the globe, *J. Geophys. Res.*, *81*, 3719–3724.

Rumelhart, D. E., G. E. Hinton, and R. J. Williams (1986), Learning internal representations by error propagation, in *Parallel Distributed Processing: Explorations in the Macrostructure of Cognition*, vol. 1, edited by D. E. Rumelhart and McClelland, pp. 318–362, MIT Press, Cambridge, Mass.

Salisbury, J. W., B. Hapke, and J. W. Eastes (1987), Usefulness of weak bands in mid- infrared remote sensing of particulate planetary surfaces, *J. Geophys. Res.*, *92*, 702–710.

Salisbury, J. W., L. S. Walter, N. Vergo, and D. M. D'Aria (1991), *Infrared (2.1–25 Micrometers) Spectra of Minerals*, 294 pp., Johns Hopkins Univ. Press, Baltimore, Md.

Scott, N. A., and A. Chédin (1981), A fast line-by-line method for atmospheric absorption computation: The Automatized Atmospheric Absorption Atlas, *J. Appl. Meteorol.*, *20*, 801–812.

Scott, N. A., et al. (1999), Characteristics of the TOVS pathfinder path-B dataset, *Bull. Am. Meteorol. Soc.*, *80*, 2679–2701.

Smith, W. L., H. M. Woolf, C. S. Wofsy, and L. M. McMillin (1979), The TIROS-N operational vertical sounder, *Bull. Am. Meteorol. Soc.*, *60*, 1177–1187.

Stubenrauch, C. J., N. A. Scott, and A. Chédin (1996), Cloud field identification for Earth radiation budget studies. Part 1: Cloud field classification using HIRS-MSU sounder measurements, *J. Appl. Meteorol.*, *35*, 416–427.

Stubenrauch, C. J., W. B. Rossow, F. Cheruy, A. Chédin, and N. A. Scott (1999), Clouds as seen by satellite sounder (3I) and imagers (ISCCP). Part I: Evaluation of cloud parameters, *J. Clim.*, *12*, 2189–2213.

Uddstrom, M. J., and L. M. McMillin (1994), System noise in the NESDIS TOVS Forward Model, part I: Specification, *J. Appl. Meteorol.*, *33*, 919–938.

Wahiche, C., N. A. Scott, and A. Chédin (1986), Cloud detection and cloud parameters retrieval from the satellites of the TIROS-N series, *Ann. Geophys.*, *Ser. B*, *4*(2), 207–222.

A. Chédin, E. Péquignot, N. A. Scott, and S. Serrar, Laboratoire de Météorologie Dynamique, Institut Pierre-Simon Laplace, Ecole Polytechnique, Palaiseau 91128, France. (chedin@lmd.polytechnique.fr)